ENVIRONMENTAL RESEARCH
LETTERS

LETTER • OPEN ACCESS

Meteorological conditions contributed to changes in dominant patterns of summer ozone pollution in Eastern China

Environmental Research Letters

LETTER

Meteorological conditions contributed to changes in dominant patterns of summer ozone pollution in Eastern China

Zhicong Yin[1,2,3] and Xiaoqing Ma[1]

[1] Key Laboratory of Meteorological Disaster, Ministry of Education/Joint International Research Laboratory of Climate and Environment Change (ILCEC)/Collaborative Innovation Center on Forecast and Evaluation of Meteorological Disasters (CIC-FEMD), Nanjing University of Information Science & Technology, Nanjing 210044, People's Republic of China
[2] Southern Marine Science and Engineering Guangdong Laboratory (Zhuhai), Zhuhai, People's Republic of China
[3] Nansen-Zhu International Research Centre, Institute of Atmospheric Physics, Chinese Academy of Sciences, Beijing, People's Republic of China

E-mail: yinzhc@163.com

Keywords: ozone, air pollution, western Pacific subtropical high, East Asian deep trough, photochemical reaction

Supplementary material for this article is available online

OPEN ACCESS

RECEIVED
8 August 2020

REVISED
6 November 2020

ACCEPTED FOR PUBLICATION
10 November 2020

PUBLISHED
15 December 2020

Abstract

Ground-level O_3 pollution has become one of the most consequential air quality problems in China. Many previous studies have addressed the increasing trend of surface O_3 concentrations in Eastern China. In this study, a new feature, i.e. the change in the dominant patterns of surface O_3, was revealed, and the associated physical mechanisms were analyzed. The impacts of meteorological conditions and anthropogenic emissions were separated, and the change in the O_3 dominant pattern was found to be mainly due to the variability in the meteorological conditions. From 2017 to 2019, the stable confrontation of the western Pacific subtropical high (WPSH) and East Asian deep trough (EADT) was closely related to the south-north covariant pattern of O_3, because the variability in the meteorological conditions centered on the North China and Huanghuai regions. In the period of 2015–2016, the joint movements of the WPSH and EADT modulated the meteorological anomalies, creating a dipole mode in Eastern China that contributed to out-of-phase variations in O_3 in North China and the Yangtze River Delta.

1. Introduction

At the beginning of 2013, the central government of China enacted and executed many measures to improve air quality (Xue *et al* 2019). As expected, the concentrations of fine particulate matter ($PM_{2.5}$) substantially declined (Wei *et al* 2017, Li *et al* 2019b), which brought large health and economic benefits (Chen *et al* 2017, Xue *et al* 2019). However, the concentrations of surface ozone showed contrasting trends and resulted in severe photochemical pollution in summer (Tang *et al* 2018, Wang *et al* 2020). Surface O_3 levels that exceeded the standard damaged human health (Felzer 2020, Stenke 2020) and weakened net primary productivity (Yue *et al* 2017) in Eastern China. In addition to the increasing trend and related negative impacts, the dominant patterns of daily ground-level O_3 also changed in Eastern China in recent years (Yin *et al* 2019a). From 2014 to 2016, summer ozone pollution showed a south-north differential (D_{SN}) pattern with two centers in North China (NC) and Yangtze River Delta (YRD). However, the dominant patterns shifted to a south-north covariant (C_{SN}) pattern and was centered in North China and the Huanghuai region (NCH) in 2017 and 2018. This feature was preliminarily revealed, but the reasons driving this transition of the dominant patterns are still unclear.

The variability in surface O_3 was determined by the joint effects of emissions and meteorological conditions. As revealed by many previous studies, anthropogenic emissions have played important roles in the long-term trend of ozone pollution (Zhang *et al* 2014, Li *et al* 2019a). Numerical experiments using an up-to-date regional chemical transport model showed that the causes of increasing O_3 due to changes in anthropogenic emissions varied geographically (Liu and Wang 2020). After removing the components regressed by meteorological variables, Zhu *et al* (2019) found that the increasing

trend of O_3 in NC was largely explained by decreases in $PM_{2.5}$, which slowed down the sink of hydroperoxy radicals. The increase in surface O_3 in YRD could be attributed to a reduction in nitrogen oxide (NOx) emissions and an increase in the release of volatile organic compounds (VOCs) (Yu *et al* 2019). Two kinds of the most important precursors, NOx and VOCs, were largely emitted in the economically developed regions from NC to the YRD (figures S1(a) and (b), which are available online at https://stacks.iop.org/ERL/15/124062/mmedia). Because the economic pattern in Eastern China has been relatively stable, the map of emitted VOCs and NOx did not significantly change in the recent 10 years, indicated by high spatial correlation coefficients for 4080 grids cells (figure S1(c)). Therefore, the variations in anthropogenic emissions mainly influenced the long-term temporal trend in the surface O_3 and the perennial locations of severe air pollution but had difficulty determining the changes in daily O_3-polluted modes.

Meteorological conditions play important roles in variations in ground-level O_3 from daily to interannual time scales. As a major teleconnection pattern in the Northern Hemisphere, the positive phase of Eurasia pattern can modulate the local meteorological conditions to enhance the photochemical reactions, thereby increase the ozone concentration in NC (Yin *et al* 2019b). The East Asian summer monsoon were also significantly influenced the interannual variations in surface O_3 pollution in China (Yang *et al* 2014). On a daily time scale, severe heat waves in summer frequently resulted in severe O_3 pollution in the YRD (Pu *et al* 2017). The western Pacific subtropical high (WPSH) stronger than its summer climate mean is closely related to the presence of environmental conditions that are not conducive to ozone formation, such as higher humidity, more cloud cover, less solar radiation and lower air temperature in the YRD (Zhao and Wang 2017). Photochemical production was shown to be enhanced between 800 hPa and 900 hPa above NC on dry and sunny days, and the formed O_3 was transported to the surface by downward air flow related to anticyclonic circulations at 500 hPa (Gong and Liao 2019, Dong *et al* 2020). The meteorological conditions associated with two dominant patterns (i.e. C_{SN} and D_{SN} patterns) were also modulated by large-scale atmospheric circulations, such as the WPSH and East Asian deep trough (EADT).

Although the changes in dominant patterns of daily O_3 pollution were preliminarily uncovered, the robustness of these transitions and the reasons have not yet been analyzed, to the best of our knowledge. In this study, we aimed to verify the roles of daily meteorological conditions in the change from D_{SN} to C_{SN} and the associated physical mechanisms. The remainder of this paper is organized as follows. The data and methods are described in section 2. Section 3.1 confirms the change in the dominant O_3 patterns and the roles of meteorological conditions through observational and numerical approaches. Then, the possible physical mechanisms are examined in section 3.2. The main conclusions and necessary discussions are included in section 4.

2. Datasets and methods

2.1. Data descriptions

The hourly ozone concentration data since May 2014 are publicly available at https://www.aqistudy.cn/historydata/ (last access: 12 April 2020). The number of observation sites in 2014 was much fewer than that at later dates; thus, we used the ozone data from 2015 to 2019 to analyze the dominant patterns of the maximum daily 8 h average ozone concentrations (MDA8 O_3). The sites with more than 5% of the data missed were eliminated, and then 660 sites in Eastern China were employed in this study. The NOx and VOCs data were emissions data from the Multi-resolution Emission Inventory for China, which can be downloaded from the website of www.meicmodel.org.

The daily atmospheric data employed in the stepwise multiple linear regression (MLR) are listed in table S1; the variables included surface air temperature (SAT) and relative humidity (RH), 10 m zonal and meridional wind (u10m and v10m), boundary layer height, precipitation, low and medium cloud cover (mlcc), 850 hPa meridional wind, and sea level pressure. These reanalysis data, with a resolution of $0.125° \times 0.125°$, were provided by the fifth generation European Center for Medium-Range Weather Forecasts reanalysis dataset (Copernicus Climate Change Service 2017). Furthermore, the zonal and meridional wind, geopotential height, RH, and vertical velocity at different vertical levels and downward solar radiation at the surface were also used to analyze the associated atmospheric circulations.

2.2. Quantifying contributions of meteorological conditions according to MLR

A number of previous studies have examined the meteorological influences on air pollution in China (Li *et al* 2019a, Yin *et al* 2019b) and decomposed the impacts of meteorological conditions and anthropogenic emissions with a MLR approach (Zhai *et al* 2019). In this study, we also constructed a stepwise MLR model with the highly correlated meteorological variables at each measured site. That is, the regression values were identified as the impacts of meteorological conditions on surface ozone (MDA8 O_3M), and the residual differentials were the effects of anthropogenic emissions (MDA8 O_3R, equation (1)). Nine of the significantly correlated meteorological variables were considered candidates (table S1) and then were severally selected by the stepwise MLR at each station (equation (2)). To focus on synoptic-scale variability, all data (X_k and MDA8 O_3) were deseasonalized by

subtracting the 30 d moving averages from the original data for each year (Tai *et al* 2012), and the linear trend was synchronously removed (Zhai *et al* 2019).

$$\text{MDA8 O}_3 = \text{MDA8 O}_3\text{M} + \text{MDA8 O}_3\text{R} \quad (1)$$

$$\text{MDA8 O}_3\text{M}_i(t) = \sum_{k=1}^{9} \beta_{i,k} X_{i,k}(t) + b_i \quad (2)$$

where MDA8 O_3M_i (t) is the regressed ozone time series for station i, and $X_{i,k}$ (t) is the corresponding time series for the deseasonalized and detrended meteorological variables. The MDA8 O_3R component cannot be explained by the MLR model and includes variability mainly attributed to changes in anthropogenic emissions (Pei *et al* 2020) and possible noise due to limitations of MLR. In order to examine the possible multicollinearity problem, the variance inflation factor of each developed MLR model were calculated (Kutner *et al* 2004). The largest variance inflation factor is less than 4.5, therefore, the multicollinearity problem is insignificant. To avoid overfitting, we also tried to limit the largest number of input factors in the stepwise MLR model to three (Leung *et al* 2018, Li *et al* 2019a), and the results are consistent with the former.

2.3. Simulating surface O_3 with fixed emissions by GEOS–Chem

The hourly ozone concentrations were also simulated with the nested-grid version of the global 3D chemical transport model (GEOS–Chem) with detailed oxidant–aerosol chemistry and driven by MERRA-2 assimilated meteorological data (Gelaro *et al* 2017). This model used dry deposition velocity to compute the ozone concentration at a given altitude (such as 10 m) above the surface so that the simulated data could be compared with the data from the observational network (Travis and Jacob 2019). The emissions data for 2010 were downloaded from the website of http://geoschemdata.computecanada.ca/ExtData/HEMCO/AnnualScalar. The ozone simulations were configured with a horizontal resolution of $0.5^\circ \times 0.625^\circ$ nested grid over East Asia and driven by changing meteorological fields from 2015 to 2019 but with fixed emissions in 2010. Thus, the annual differences of simulated O_3 solely resulted from the changes of meteorology-related processes rather than anthropogenic emissions.

The ozone concentration is determined by several physical–chemical processes. We used non-local planetary boundary layer (PBL) mixing in the simulation, so the emissions and dry deposition trends within the PBL were applied within the mixing (Holtslag and Boville 1993). Wet deposition was not considered because of its small contribution to the O_3 mass flux (Liao *et al* 2006). Thus, in the analysis of the physical–chemical processes related to meteorological conditions, the chemistry, convection, PBL mixing, transport and their sum within the PBL were the focus.

2.4. Extracting the dominant patterns by EOF

The empirical orthogonal function (EOF) is to decompose the original data into orthogonal basis functions, including spatial and temporal coefficients and corresponding variance contribution (North *et al* 1982). In the spatial pattern of EOF, the sites with large spatial coefficient are the center of daily variability where the decomposed values frequently and largely varied from their mean state. In our research, the EOF analysis was applied to the daily observations of MDA8 O_3 in Eastern China from 2015 to 2019, and was also applied to the simulated MDA8 O_3 to compared with the results of the observational results. Because the O_3 variability was purely produced by changing meteorological conditions in the numerical simulations, the change in dominant patterns of simulated MDA8 O_3 was influenced by meteorological contributions. In this study, we used the test method from North *et al* (1982) to verify the significance of the separated EOF patterns. That is, if the eigenvalue (λ_i) of the ith mode satisfied the condition $\lambda_i - \lambda_{i+1} \geq \lambda_i(2/n)^{1/2}$, the eigenvalue λ_i was significantly separated.

3. Results

3.1. Changes in dominant O_3 patterns

As illustrated by Yin *et al* (2019a), two dominant patterns of summer ozone pollution were determined based on the observations from 2015 to 2018. The first prominent pattern changed synergistically in Eastern China and the second pattern showed remarkable south-north differences. When the range of data was extended to 2019, these two patterns were also significant (passing the North test), with variance contributions of 25% and 12.9% for the first (C_{SN} pattern) and second (D_{SN} pattern) EOF modes, respectively (figures 1(a) and (b)). In the C_{SN} pattern, the daily MDA8 O_3 in Eastern China covaried (figure 1(a)) and was centered on NCH. However, the variation in MDA8 O_3 showed features that varied between the south and north and was centered on NC and YRD in the D_{SN} pattern (figure 1(b)). These first two patterns were successfully reproduced by GEOS–Chem model driven by the meteorology from 2015 to 2019 and fixed emissions (figure omitted). Similar EOF analyses were also executed for the observed MDA8 O_3 in each year from 2015 to 2019. It was obvious that the first EOF mode was similar to the D_{SN} pattern in 2015 and 2016 and was similar to the C_{SN} pattern from 2017 to 2019 (figure S2). The spatial correlation coefficients between the two dominant patterns and the first EOF mode in each year were calculated and are shown in figure 1(c). The high spatial correlation

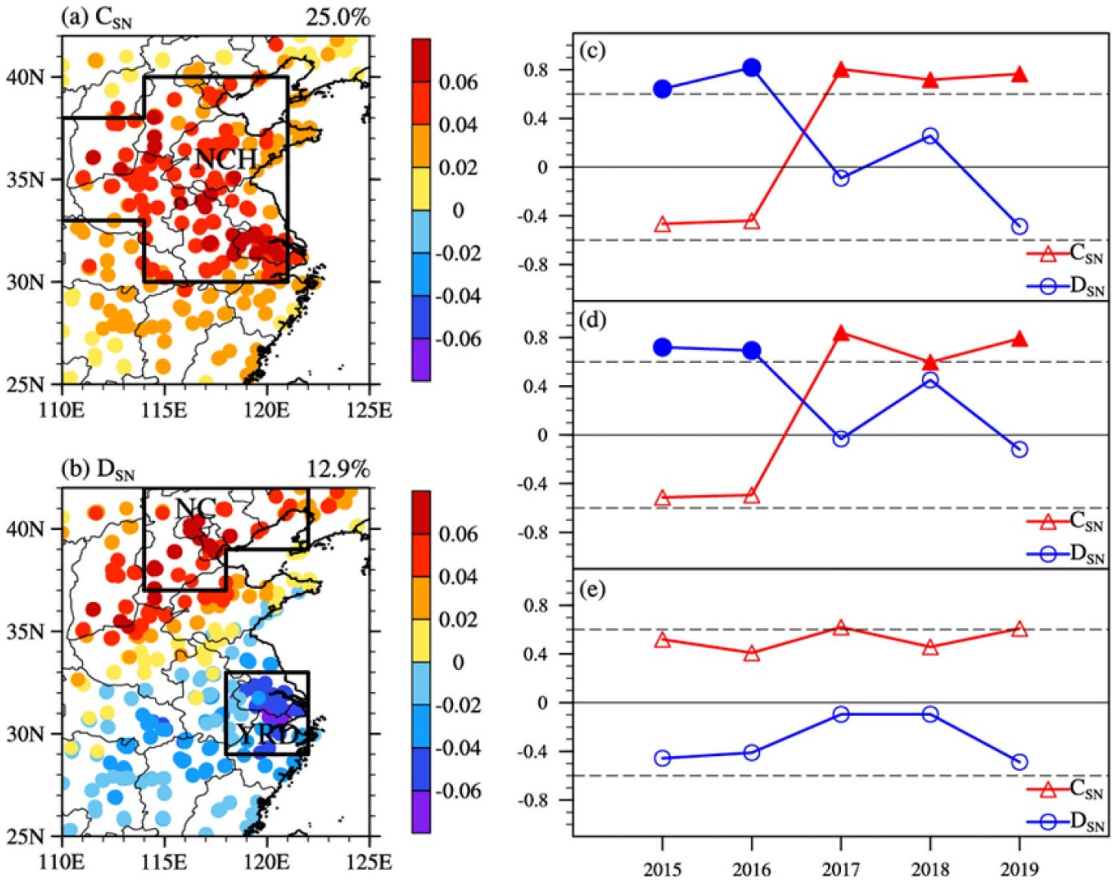

Figure 1. The first (a) and second (b) EOF spatial patterns of observed MDA8 O_3 in summer from 2015 to 2019. EOF analysis was applied to the MDA8 O_3 after subtracting the 30 d moving averages from the original data. The percentages in panels are the variance contributions. The first and second EOF patterns for 5 years were defined as C_{SN} and D_{SN}, respectively. The black boxes in panels (a) and (b) indicate the locations of NCH, NC and YRD. Spatial correlation coefficient between the C_{SN} (red) and the first EOF patterns of each year from 2015 to 2019, between D_{SN} (blue) and the first EOF patterns. In panels (c–e), the EOF pattern in each year was decomposed from the observed MDA8 O_3 (c), MDA8 O_3M (d) and MDA8 O_3R (e). Solid circles and triangles indicate that the absolute value of the spatial correlation coefficient was above 0.6.

coefficients (>0.6) confirmed that the most dominant mode in 2015 and 2016 was the D_{SN} pattern, which then shifted to the C_{SN} pattern (figure 1(c)).

As mentioned above, the concentrations of O_3 were significantly correlated with the meteorological conditions, and the top meteorological predictors in the MLR varied geographically (Li *et al* 2019a). In this study, we performed stepwise regression on the deseasonalized and detrended MDA8 O_3 at each site using the meteorological variables in table S1. The coefficient of determination (R^2, fraction of variance explained) was used to describe the ability of the optimized MLR to reproduce the variability in the observed MDA8 O_3 (figure S3). The 5 years averaged values of R^2 for the NC, YRD and NCH were 0.51, 0.45 and 0.46, respectively, indicating good performance. The fitted values were the O_3 components influenced by meteorological conditions and were denoted as MDA8 O_3M. In Beijing (largest city in NC), the correlation coefficient between the observed MDA8 O_3 and MDA8 O_3M was above 0.76 in each year, exceeding the 99% confidence level (figure 2(a)). In the largest city of the YRD (Shanghai), this correlation coefficient was above 0.68 and exceeded the 99% confidence level (figure 2(b)).

The dominant patterns of the MDA8 O_3M and associated meteorology were diagnosed basing on the full period (2015–2019) and two sub-periods (2017–2019 and 2015–2016), respectively. The results well agreed each other. Therefore, in order to enhance the signals of the most important mode and explore the reasons for the changes in dominant patterns, the MDA8 O_3M was decomposed by the EOF method for the period of 2017–2019 and 2015–2016, respectively. The first EOF mode of MDA8 O_3M in these two periods resembled the C_{SN} and D_{SN} pattern and was defined as the C_{SN}M and D_{SN}M pattern (figures 3(a) and (b)). The spatial correlation coefficients were 0.81 (between the C_{SN}M and C_{SN} pattern) and 0.74 (between the D_{SN}M and D_{SN} pattern), indicating that the meteorological conditions possibly contributed to the distributions of the dominant patterns of surface ozone pollution in Eastern China. With fixed emissions, the O_3 concentrations were simulated by the GEOS–Chem model with meteorological conditions from 2015 to 2019. In this experiment, the

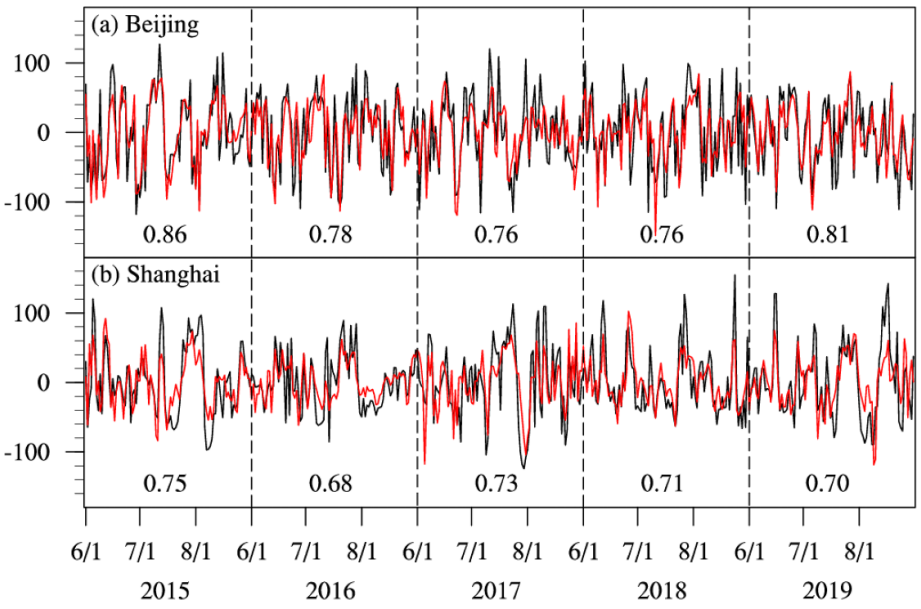

Figure 2. Variations in the observed MDA8 O_3 (unit: $\mu g\ m^{-3}$, black) and fitted MDA8 O_3M (unit: $\mu g\ m^{-3}$, red) after subtracting the 30 d moving averages from the original data in (a) Beijing (located in NC) and (b) Shanghai (located in YRD). The correlation coefficients between the observed MDA8 O_3 and fitted MDA8 O_3M in each year are also presented.

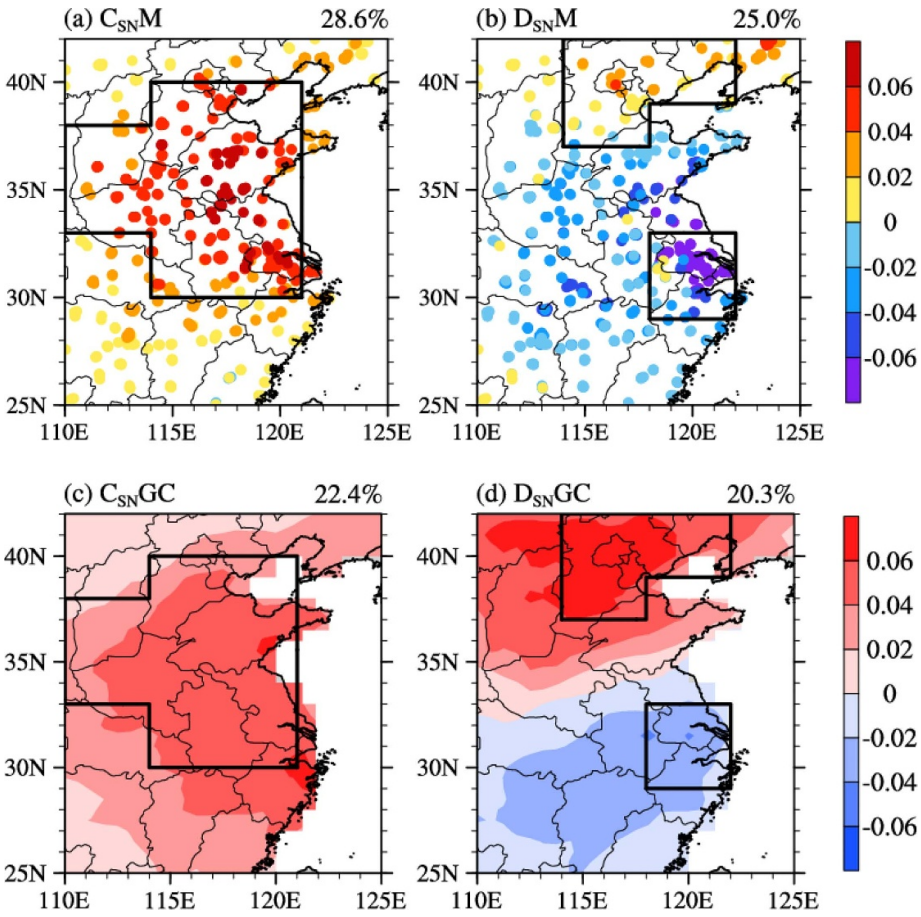

Figure 3. The first EOF pattern of the fitted MDA8 O_3M from 2017 to 2019 (a) and from 2015 to 2016 (b). The first EOF pattern of simulated MDA8 O_3 from 2017 to 2019 (c) and from 2015 to 2016 (d) are also shown. The simulated O_3 concentrations were produced by GEOS–Chem with fixed emissions but changing meteorological conditions. The percentages are the variance contributions of the first EOF mode. The black box in panels (a) and (c) indicates the location of NCH, while those in panels (b) and (d) are the NC and YRD areas.

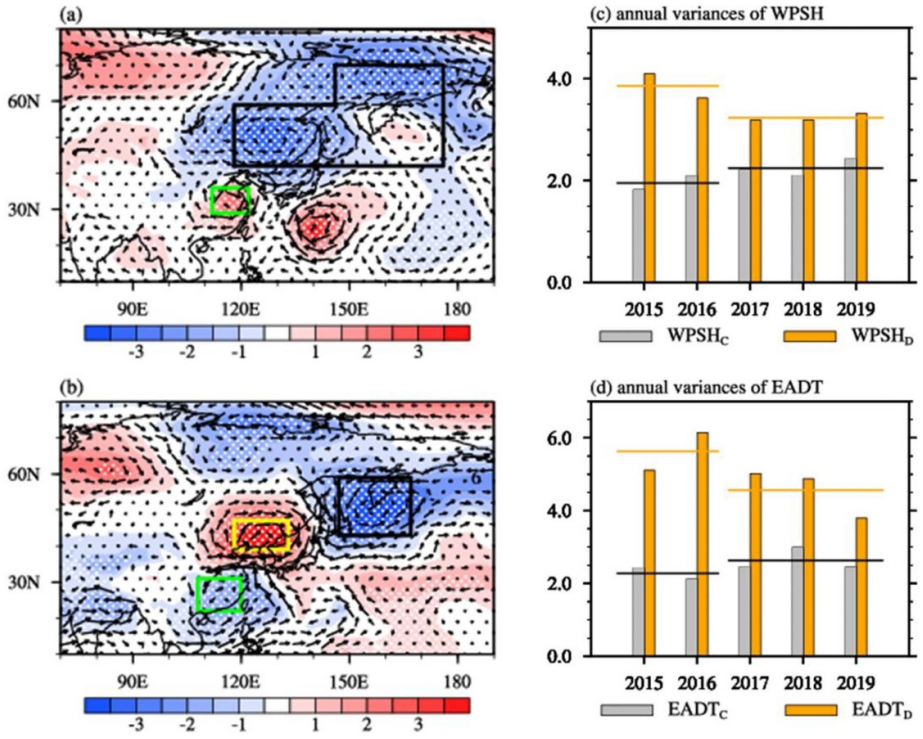

Figure 4. Composites of the daily geopotential height at 850 hPa (unit: 10 gpm, contours) and horizontal wind at 850 hPa (unit: m s^{-1}, arrows) associated with the first EOF pattern of MDA8 O_3M (a) from 2017 to 2019 (i.e. positive C_{SN}M minus negative C_{SN}M) and (b) from 2015 to 2016 (i.e. positive D_{SN}M minus negative D_{SN}M). The white dots indicate that the differences with shading was above the 95% confidence level. The $WPSH_C$ and $WPSH_D$ indicated the location of the WPSH, whose annual variance (unit: 10 gpm) is shown in panel (c). The $WPSH_C$ is defined as area-averaged Z850 (29–36° N, 112–122° E; green box in panel a), and the $WPSH_D$ represents the area-averaged differences in Z850 (the yellow box minus the green box in panel b; 39–47° N, 118–133° E, yellow box; 22–31° N, 108–120° E, green box). $EADT_C$ and $EADT_D$ indicate the location of the EADT, and the annual variance (unit: 10 gpm) is shown in panel (d). $EADT_C$ is defined as the area-averaged Z850 (42–59° N, 118–146° E; 42–70° N, 146–176° E; black box in panel a), and $EADT_D$ represents the area-averaged differences in Z850 (the black box minus the yellow box in panel b; 43–59° N, 147–167° E, black box; 39–47° N, 118–133° E, yellow box).

variability in O_3 was solely produced by the meteorological conditions. The deseasonalized and detrended MDA8 O_3 in this simulation had a high correlation with the observed values (i.e. approximately 0.7 in Beijing and approximately 0.75 in Shanghai), indicating good performance of GEOS–Chem in reproducing the synoptic variability in O_3 (figure S4). The C_{SN} and D_{SN} patterns of MDA8 O_3 were successfully reproduced (figures 3(c) and (d)), which verified the roles of meteorological conditions in determining the dominant patterns of daily MDA8 O_3.

Can meteorological conditions influence the change in dominant patterns of surface ozone pollution in Eastern China? That is, whether the EOF results of MDA8 O_3M also changed from the D_{SN} pattern from 2015 to 2016 to the C_{SN} pattern since 2017 should be examined. As expected, the first EOF mode shifted from the D_{SN} to the C_{SN} pattern in the 5 years (figure S5), which was further verified by the calculated spatial correlation coefficients, which are shown in figure 1(d). The correlation coefficient between the first EOF mode and D_{SN} pattern was significant (above 0.6) from 2015 to 2016 but dramatically declined after that. However, the correlation coefficient with the C_{SN} pattern increased to become significant starting in 2017 (figure 1(d)). The MDA8 O_3R (i.e. MDA8 O_3−MDA8 O_3M, equation (1)) was mainly related to changes in anthropogenic emissions (Zhai *et al* 2019, Li *et al* 2019a), whose EOF mode remained almost unchanged from 2015 to 2019 (figure S6) and had weak spatial correlations with both the D_{SN} and C_{SN} patterns (figure 1(e)). In addition, the dominant pattern of MDA8 O_3R resembled the distributions of the NOx and VOCs emissions (figure S1), indicating a close relationship between them.

3.2. Associated physical mechanisms

In the former section, by separating the contributions of anthropogenic emissions and meteorological conditions, we speculated that the change in the dominant patterns of surface ozone pollution in Eastern China was mainly driven by the variability in meteorological conditions. In this section, we attempted to analyze the associated physical mechanisms. For both the C_{SN}M and D_{SN}M patterns, the time series exceeding 1 (lower than −1) standard deviation were defined as their positive (negative) phase (figure S7). The associated large-scale atmospheric circulations and meteorological conditions were composited

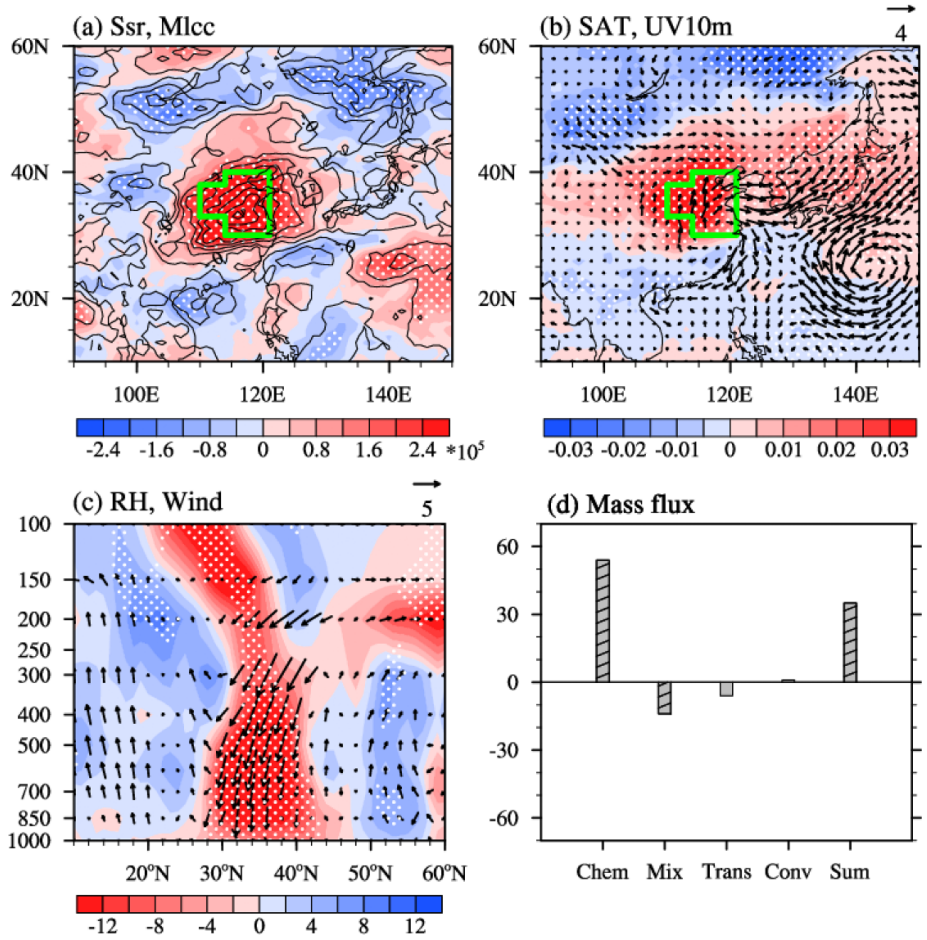

Figure 5. Composites of the daily atmospheric circulations associated with the first EOF pattern of MDA8 O_3M from 2017 to 2019 (i.e. positive C_{SN}M minus negative C_{SN}M): (a) downward solar radiation at the surface (unit: 10^5 J m^{-2}, shading) and the sum of mlcc (unit: 1, contours), (b) surface wind (unit: m s^{-1}, arrows) and SAT (unit: K, shading), and (c) 110–130° E mean wind (unit: m s^{-1}, arrows) and RH (unit: %, shading). The white dots indicate that the differences with shading was above the 95% confidence level. The green boxes in panels (a) and (b) are the NCH regions. Composites of the daily mass fluxes of ozone (d) associated with the first EOF pattern of MDA8 O_3M for (a), (b) the NCH-averaged from 2017 to 2019 (i.e. positive C_{SN}M minus negative C_{SN}M). The bottom axis in panel (d) is the name of the physical-chemical processes: chemical reaction (Chem), PBL mixing (Mix), transport (Trans), convection (Conv) and their sums (Sum), unit: Tons d^{-1}. The mass fluxes were simulated by GEOS–Chem and were calculated within the planetary boundary layer. The black slashes indicate that the composite results were above the 95% confidence level.

as the differences between the positive and negative phases (positive minus negative) to explore the reasons for the change in the dominant patterns of O_3.

According to the positive (negative) phase of C_{SN}M, the positive (negative) MDA8 O_3M was concentrated in the NCH region (figures S8(a) and (b)). Anomalous anticyclonic circulations were located above the NCH region in the middle (figure S9(a)) and lower (figure 4(a)) troposphere and resulted in downward air flow from the stratosphere to the near surface (figure 5(c)). The transport of O_3 from the stratosphere to the surface was an important way to elevate the concentrations of surface O_3 (Langford *et al* 2009). On the other hand, the significant descending air flows indicated efficient adiabatic heating (resulting in high SAT, figure 5(b)) and dry air below 300 hPa (figure 5(c)). Furthermore, mlcc were significantly reduced, which allowed intense solar radiation to enhance the photochemical reactions (figure 5(a)). The produced O_3 could be transported to the surface by downward air flow related to anticyclonic circulations (Gong and Liao 2019). The composite results from GEOS–Chem also verified the impacts of the meteorological conditions. The chemical reactions had large positive values (54.7 Tons d^{-1}), and the sum of all physical–chemical processes was 35.1 Tons d^{-1}, resulting in more O_3 (figure 5(d)). Therefore, the negative and positive phases of the abovementioned meteorological conditions significantly influenced the variability in the MDA8 O_3M in the NCH regions.

The MDA8 O_3M for the positive and negative phases of the D_{SN}M pattern had similar centers (i.e. NC and YRD) but presented opposite signs (figures S8(c) and (d)). The adjacent cyclonic and anticyclonic anomalies were located over the YRD and NC in the middle (figure S9(b)) and lower (figure 4(b)) troposphere, inducing ascending and

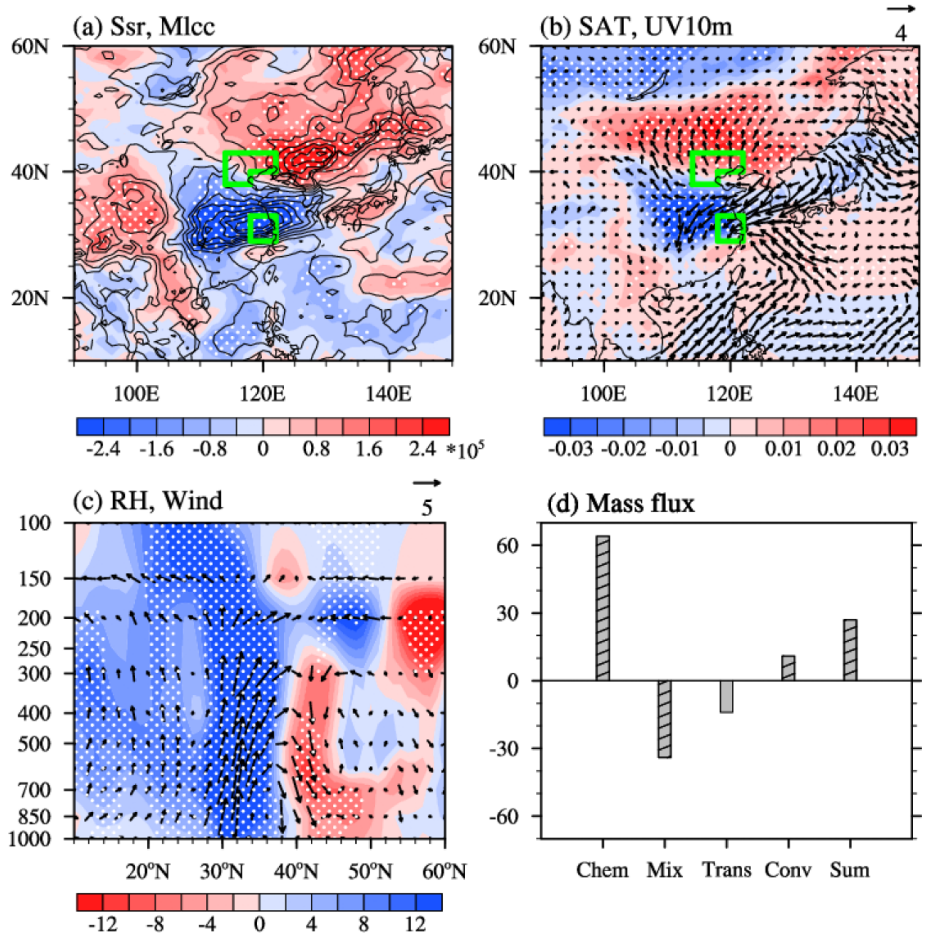

Figure 6. Composites of the daily atmospheric circulations associated with the first EOF pattern of MDA8 O_3M from 2015 to 2016 (i.e. positive D_{SN}M minus negative D_{SN}M): (a) downward solar radiation at the surface (unit: 10^5 J m^{-2}, shading) and the sum of mlcc (unit: 1, contours), (b) surface wind (unit: m s^{-1}, arrows) and SAT (unit: K, shading), and (c) 110–130° E mean wind (unit: m s^{-1}, arrows) and RH (unit: %, shading). The white dots indicate that the differences with shading was above the 95% confidence level. The green boxes in panels (a) and (b) are the NC and YRD regions. Composites of the daily and mass fluxes of ozone (d) associated with the first EOF pattern of MDA8 O_3M for the area-averaged differences (NC minus YRD) from 2015 to 2016 (i.e. positive D_{SN}M minus negative D_{SN}M). The bottom axis in panel (d) is the name of the physical-chemical processes: chemical reaction (Chem), PBL mixing (Mix), transport (Trans), convection (Conv) and their sums (Sum), unit: Tons d^{-1}. The mass fluxes were simulated by GEOS–Chem and were calculated within the planetary boundary layer. The black slashes indicate that the composite results were above the 95% confidence level.

descending motions (figure 6(c)), respectively. The contrast between the meteorological conditions in NC and the YRD was stark, i.e. hot–dry in NC but cool–moist in the YRD (figures 6(b) and (c)). More importantly, the photochemical production of O_3 in NC was significantly enhanced but was restrained in the YRD by the variability in solar radiation (figure 6(a)). The GEOS–Chem simulations also confirmed the stark contrast of the chemical reactions related to the meteorological conditions. The hot-dry environments in NC resulted in chemical reactions that were 64.8 Tons d^{-1} stronger than those in the cool-moist air in the YRD (figure 6(d)). Thus, the differences in meteorological conditions between the NC and YRD played important roles in the formation of the D_{SN}M pattern.

As illustrated in figures 4(a) and (b), the configurations of WPSH and EADT were closely related to the distribution of MDA8 O_3M in Eastern China. The WPSH occupied the east of China, and the EADT was stronger and extended to the Korean Peninsula for the positive phase of C_{SN}M, and vice versa. These two large-scale atmospheric circulations stably confronted each other and resulted in persistent changing centers of meteorological conditions in NCH. The $WPSH_C$ index was defined as the area-averaged geopotential height at 850 hPa (Z850) in the Huai River region (29–36° N, 112–122° E; green box in figure 4(a)), and the $EADT_C$ index was calculated as the area-averaged Z850 in Northeast China (42–59° N, 118–146° E; 42–70° N, 146–176° E; black box in figure 4(a)). The annual variances of $WPSH_C$ and $EADT_C$ from 2017 to 2019 were larger than those from 2015 to 2016 (figures 4(c) and (d)), indicating that these two key factors frequently fluctuated and effectively modulated the local metrological conditions. Therefore, the stable confrontation of WPSH and EADT showed that the variations in meteorological conditions presented features associated with the C_{SN}M pattern of

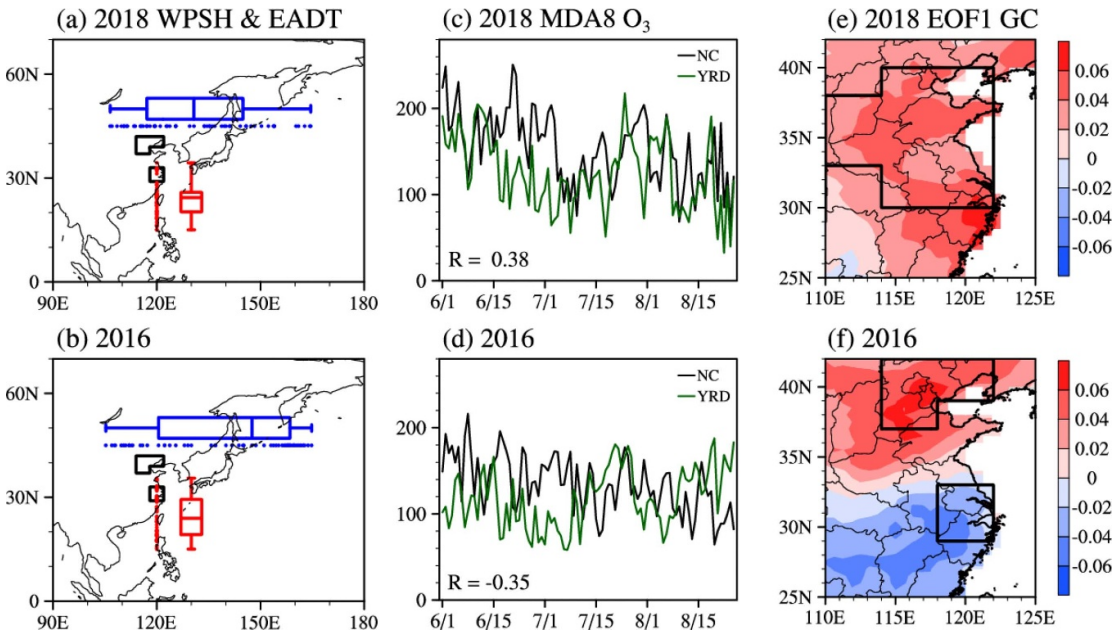

Figure 7. The WPSH ridge line at 120° E (red spots) and the EADT axis at 45° N (blue spots) and their statistical boxplots in 2018 (a) and 2016 (b). The bottom and top edges of the boxes are the 25th and 75th percentiles, respectively. The whiskers extend from the minimum to the maximum values. Variations in the MDA8 O_3 (unit: $\mu g\ m^{-3}$) of NC (black) and YRD (green) in 2018 (c) and 2016 (d). The first EOF spatial patterns simulated by the GEOS–Chem model MDA8 O_3 in summer 2018 (e) and 2016 (f). The GEOS–Chem model was driven by meteorological fields in summer 2018 and 2016 and fixed emissions. The black boxes in panels (a), (b), (e), and (f) indicate the locations of NCH, NC and YRD, respectively.

MDA8 O_3 in Eastern China. In contrast, the WPSH and EADT, which were associated with the $D_{SN}M$ pattern, mutually advanced and retreated. For the positive phase of the $D_{SN}M$ pattern, the WPSH moved northward, and the EADT receded to Okhotsk (figure 4(b)). To include information on systematic movement, the $WPSH_D$ index was defined as the area-averaged difference in Z850 between Northeast China and South China (the yellow box minus the green box in figure 4(b); 39–47° N, 118–133° E, yellow box; 22–31° N, 108–120° E, green box), and the $EADT_D$ index was also calculated as the area-averaged difference in Z850 between the Kamchatka Peninsula and Northeast China (the black box minus the yellow box in figure 4(b); 43–59° N, 147–167° E, black box; 39–47° N, 118–133° E, yellow box). The annual variances of $WPSH_D$ and $EADT_D$ were stronger from 2015 to 2016 (figures 4(c) and (d)), meaning the WPSH and EADT during this period advanced and retreated more frequently and resulted in the $D_{SN}M$ pattern of MDA8 O_3 in Eastern China.

The configuration of WPSH and EADT showed features of mutual movements from 2015 to 2016, modulating the meteorological conditions to represent a dipole mode and contributing to the $D_{SN}M$ pattern of MDA8 O_3 in Eastern China. However, the stable confrontation of WPSH and EADT resulted in a monopole mode of the meteorological conditions and determined the $C_{SN}M$ pattern of MDA8 O_3 from 2017 to 2019. Similar to Yin *et al* (2019a), the years 2016 and 2018, when the dominant modes were clearly separated (because the variance contribution of the first EOF mode was almost twice that of the second pattern), were selected as two cases to examine the rationality of the above physical mechanisms. The latitude corresponding to the WPSH ridge line at 120° E and the longitude corresponding to the EADT axis at 45° N were extracted to quantify the daily variability in the positions of these two key factors. The standard deviation of the WPSH ridge position was 4.9 degrees in 2018 and was 22% stronger in 2016 (i.e. 6 degrees). Similarly, the standard deviation of the EADT axis position in 2016 was also stronger than that in 2018 (figures 7(a) and (b)). The positions of the WPSH and EADT varied slightly more in 2018 and resulted in a stable changing center of meteorological conditions in NCH. The observed MDA8 O_3 in NC and the YRD varied synchronously and had a significantly positive correlation coefficient (0.38, figure 7(c)). The first EOF mode of MDA8 O_3 simulated by GEOS–Chem also showed the features of the $C_{SN}M$ pattern (figure 7(e)). In 2016, the positions of the WPSH and EADT frequently varied, leading to a stark contrast in meteorological conditions in NC and the YRD and thus out-of-phase MDA8 O_3 between NC and the YRD (the correlation coefficient between them was −0.35, exceeding the 99% confidence level, figure 7(d)). The simulated MDA8 O_3 also appeared as a $D_{SN}M$ pattern (figure 7(f)).

4. Conclusions and discussion

In this study, we confirmed that the dominant pattern of summer ozone pollution in Eastern China

changed. From 2015 to 2016, the daily ozone pollution showed differential pattern between the south and north. However, the ozone pollution in the south and north covaried after 2017 (i.e. it changed from a south–north differential pattern to a south-north covariant pattern). By separating the impacts of meteorological conditions and anthropogenic emissions, we found that the change in the O_3 dominant pattern was mainly due to the variability in the meteorological conditions. From 2017 to 2019, the WPSH and EADT stably confronted each other, and the fluctuation in their intensity resulted in variability in meteorological conditions centered on NCH. Anomalous anticyclonic circulations located above the NCH region resulted in hot–dry air and stronger photochemical reactions and transported O_3 to the surface and vice versa. These physical mechanisms dominated and forced the daily O_3 to covary in Eastern China. In the period of 2015–2016, the WPSH and EADT frequently and mutually advanced and retreated, modulating the meteorological anomalies to create a dipole mode in Eastern China. Cyclonic and anticyclonic anomalies were located over the YRD and NC and led to a stark contrast in meteorological conditions in NC and the YRD, i.e. hot–dry in NC but cool–moist in the YRD. The enhanced photochemistry in NC and restrained O_3 production in the YRD significantly contributed to the different levels of MDA8 O_3 in these two areas and vice versa. These physical mechanisms induced the daily O_3 in Eastern China to show out-of-phase variations.

O_3 observations with high resolution can be obtained from the observational network of the China Ministry of Ecology and Environment after 2014. Although there were fewer sites in 2014, Zhao and Wang (2017) reported that the O_3 pattern differed between the north and south. In total, these two dominant patterns are highlighted in the periods of 2014–2016 and 2017–2019. The positions of WPSH and EADT and their joint movements have interannual change, which contribute to the change in dominant patterns of surface ozone. The aforementioned interannual change of WPSH and EADT is also affected by some external forcings, such as sea surface temperature (Jeong *et al* 2018, Li *et al* 2020; Yu and Sun 2020) and Arctic sea ice (Guo *et al* 2014, Wu *et al* 2015), which were worthy of future studies. The time range of the observations was short and limited to revealing a long-standing relationship. A possible path was to employ the simulated O_3 concentrations by GEOS–Chem for more than three decades because this model successfully recognized these two patterns from 2015 to 2019, and the external forcing factors that lead to changes in the location of WPSH and EADT might be explained in the future. Since the emission inventory has not been updated in a timely manner after 2017, we adopted statistical methods for this study and verified our conclusions by simulations with changing meteorological fields from 2015 to 2019 and fixed emissions in 2010. If the emission inventory is updated, the simulations with variable emissions but fixed meteorological fields will illustrate more information for studying the change in dominant patterns of MDA8 O_3.

Acknowledgments

The National Natural Science Foundation of China (Grant Nos. 91744311, 41991283 and 41705058).

Data availability statement

All data that support the findings of this study are included within the article (and any supplementary information files).

References

Chen L, Shi M, Li S, Gao S, Zhang H, Sun Y, Mao J, Bai Z, Wang Z and Zhou J 2017 Quantifying public health benefits of environmental strategy of $PM_{2.5}$ air quality management in Beijing-Tianjin-Hebei region, China *J. Environ. Sci.* **57** 33–40

Copernicus Climate Change Service 2017 ERA5: fifth generation of ECMWF atmospheric reanalyses of the global climate Copernicus Climate Change Service Climate Data Store (available at: https://cds.climate.copernicus.eu/cdsapp#!/home) (Accessed 22 May 2020)

Dong Y M, Li J, Guo J P, Jiang Z J, Chu Y Q, Chang L, Yang Y and Liao H 2020 The impact of synoptic patterns on summertime ozone pollution in the North China Plain *Sci. Total Environ.* **735** 139559

Felzer B S 2020 Cleaner air is a win–win *Nat. Clim. Change* **10** 104–5

Gelaro R *et al* 2017 The modern-era retrospective analysis for research and applications version 2 (MERRA2) *J. Clim.* **30** 5419–54

Gong C and Liao H 2019 A typical weather pattern for the ozone pollution events in North China *Atmos. Chem. Phys.* **19** 13725–40

Guo D, Gao Y, Bethke I, Gong D, Johannessen O and Wang H 2014 Mechanism on how the spring Arctic sea ice impacts the East Asian summer monsoon *Theor. Appl. Climatol.* **115** 107–19

Holtslag A A M and Boville B A 1993 Local versus nonlocal boundary layer diffusion in a global climate model *J. Clim.* **6** 1825–42

Jeong J I, Park R J and Yeh S W 2018 Dissimilar effects of two El Niño types on $PM_{2.5}$ concentrations in East Asia *Environ. Pollut.* **242** 1395–403

Kutner M, Nachtsheim C and Neter J 2004 *Applied Linear Regression Models* (Illinois: Richard D. Irwin Inc.)

Langford A O, Aikin K C, Eubank C S and Williams E J 2009 Stratospheric contribution to high surface ozone in Colorado during springtime *Geophys. Res. Lett.* **36** L12801

Leung D M, Tai A P K, Mickley L J, Moch J M, Donkelaar A V, Shen L and Martin R V 2018 Synoptic meteorological modes of variability for fine particulate matter ($PM_{2.5}$) air quality in major metropolitan regions of China *Atmos. Chem. Phys.* **18** 6733–48

Li H, Xu F and Lin Y 2020 The impact of SST on the zonal variability of the western Pacific subtropical high in boreal summer *J. Geophys. Res. Atmos.* **125** e2019JD031720

Li K, Jacob D J, Liao H, Shen L, Zhang Q and Bates K H 2019a Anthropogenic drivers of 2013–2017 trends in summer surface ozone in China *Proc. Natl Acad. Sci.* **116** 422–7

Li X, Song H, Zhai S, Lu S, Kong Y, Xia H and Zhao H 2019b Particulate matter pollution in Chinese cities: areal-temporal

variations and their relationships with meteorological conditions (2015–2017) *Environ. Pollut.* **246** 11–18

Liao H, Chen W T and Seinfeld J H 2006 Role of climate change in global predictions of future tropospheric ozone and aerosols *J. Geophys. Res. Atmos.* **111** D12304

Liu Y M and Wang T 2020 Worsening urban ozone pollution in China from 2013 to 2017—Part 2: the effects of emission changes and implications for multi-pollutant control *Atmos. Chem. Phys.* **20** 6305–21

North G R, Bell T L, Cahalan R F and Moeng F J 1982 Sampling errors in the estimation of empirical orthogonal functions *Mon. Weather Rev.* **110** 699–706

Pei L, Yan Z W, Chen D L and Miao S G 2020 Climate variability or anthropogenic emissions: which caused Beijing Haze *Environ. Res. Lett.* **15** 034004

Pu X, Wang T J, Huang X, Melas D, Zanis P, Papanastasio D K and Poupkou A 2017 Enhanced surface ozone during the heat wave of 2013 in Yangtze River Delta region, china *Sci. Total Environ.* **603** 807–16

Stenke A 2020 Natural control on ozone pollution *Nat. Clim. Change* **10** 101–2

Tai A P K, Mickley L J, Jacob D J, Leibensperger E M, Zhang L, Fisher J A and Pye H O T 2012 Meteorological modes of variability for fine particulate matter ($PM_{2.5}$) air quality in the United States: implications for $PM_{2.5}$ sensitivity to climate change *Atmos. Chem. Phys.* **12** 3131–45

Tang B Y, Xin J Y, Gao W K, Shao P, Su H J, Wen T X, Song T, Fan G Z, Wang S G and Wang Y S 2018 Characteristics of complex air pollution in typical cities of North China *Atmos. Ocean. Sci. Lett.* **11** 29–36

Travis K R and Jacob D J 2019 Systematic bias in evaluating chemical transport models with maximum daily 8 h average (MDA8) surface ozone for air quality applications: a case study with GEOS-Chem v9.02 *Geophys. Model Dev.* **12** 3641–8

Wang Y H *et al* 2020 Contrasting trends of $PM_{2.5}$ and surface-ozone concentrations in China from 2013 to 2017 *Natl Sci. Rev.* **7** 1331–1339

Wei Y, Li J, Wang Z F, Chen H S, Wu Q Z, Li J J, Wang Y L and Wang W 2017 Trends of surface $PM_{2.5}$ over Beijing–Tianjin–Hebei in 2013–2015 and their causes: emission controls vs. meteorological conditions *Atmos. Ocean. Sci. Lett.* **10** 276–83

Wu B, Su J and D'Arrigo R 2015 Patterns of Asian winter climate variability and links to Arctic sea ice *J. Clim.* **28** 6841–58

Xue T *et al* 2019 Rapid improvement of $PM_{2.5}$ pollution and associated health benefits in China during 2013–2017 *Sci. China Earth Sci.* **62** 1847–56

Yang Y, Liao H and Li J 2014 Impacts of the East Asian summer monsoon on interannual variations of summertime surface-layer ozone concentrations over China *Atmos. Chem. Phys.* **14** 6867–79

Yin Z C, Cao B F and Wang H J 2019a Dominant patterns of summer ozone pollution in eastern China and associated atmospheric circulations *Atmos. Chem. Phys.* **19** 13933–43

Yin Z C, Wang H J, Li Y Y, Ma X H and Zhang X Y 2019b Links of climate variability among Arctic sea ice, Eurasia teleconnection pattern and summer surface ozone pollution in North China *Atmos. Chem. Phys.* **19** 3857–71

Yu S and Sun J 2020 Potential factors modulating ENSO's influences on the East Asian trough in boreal winter *Int. J. Climatol.* **40** 5066–83

Yu Y J, Wang Z, Tao H, Meng X Y, Xie S Y and Yu H X 2019 Driving factors of the significant increase in surface ozone in the Yangtze River Delta, China, during 2013–2017 *Atmos. Pollut. Res.* **10** 1357–64

Yue X, Unger N, Harper K, Xia X, Liao H, Zhu T, Xiao J, Feng Z and Li J 2017 Ozone and haze pollution weakens net primary productivity in China *Atmos. Chem. Phys.* **17** 6073–89

Zhai S, Jacob D J, Wang X, Shen L, Li K, Zhang Y, Gui K, Zhao T and Liao H 2019 Fine particulate matter ($PM_{2.5}$) trends in China, 2013–2018: separating contributions from anthropogenic emissions and meteorology *Atmos. Chem. Phys.* **19** 11031–41

Zhang Q, Yuan B, Shao M, Wang X, Lu S, Lu K, Wang M, Chen L, Chang C C and Liu S C 2014 Variations of ground-level O_3 and its precursors in Beijing in summertime between 2005 and 2011 *Atmos. Chem. Phys.* **14** 6089–101

Zhao Z J and Wang Y X 2017 Influence of the west pacific subtropical high on surface ozone daily variability in summertime over eastern china *Atmos. Environ.* **170** 197–204

Zhu J, Chen L, Liao H and Dang R 2019 Correlations between $PM_{2.5}$ and ozone over China and associated underlying reasons *Atmosphere* **10** 352